



## Constraint effects in adhesive joint fracture

T. Pardoen<sup>a,\*</sup>, T. Ferracin<sup>a</sup>, C.M. Landis<sup>b</sup>, F. Delannay<sup>a</sup>

<sup>a</sup>*Département des Sciences des Matériaux et des Procédés, Université Catholique de Louvain, IMAP,  
Place Sainte Barbe 2, B-1348 Louvain-la-Neuve, Belgium*

<sup>b</sup>*MEMS, MS 321 Rice University, P.O. Box 1892, Houston, TX 77251, USA*

Received 19 July 2004; received in revised form 13 April 2005; accepted 26 April 2005

---

### Abstract

Constraint effects in adhesive joint fracture are investigated by modelling the adherents as well as a finite thickness adhesive layer in which a single row of cohesive zone elements representing the fracture process is embedded. Both the adhesive and the adherents are elastic–plastic with strain hardening. The bond toughness  $\Gamma$  (work per unit area) is equal to  $\Gamma_0 + \Gamma_p$ , where  $\Gamma_0$  is the intrinsic work of fracture associated with the embedded cohesive zone response and  $\Gamma_p$  is the extra contribution to the bond toughness arising from plastic dissipation and stored elastic energy within the adhesive layer. The parameters of the model are identified from experiments on two different adhesives exhibiting very different fracture properties. Most of the tests were performed using the wedge-peel test method for a variety of adhesives, adherents and wedge thicknesses. The model captures the constraint effects resulting from the change in  $\Gamma_p$ : (i) the plastic dissipation increases with increasing bond line thickness in the fully plastic regime and then decreases to reach a constant value for very thick adhesive layers; (ii) the plastic dissipation in the fully plastic regime increases drastically as the thickness of the adherent decreases. Finally, this model is used to assess a simpler approach which consists of simulating the full adhesive layer as a single row of cohesive elements.

© 2005 Elsevier Ltd. All rights reserved.

*Keywords:* Adhesion and adhesives; Crack tip plasticity; Fracture toughness; Elastic–plastic materials; Finite elements

---

\*Corresponding author. Tel.: +32 10 475134; fax: +32 10 474028.

E-mail address: [pardoen@imap.ucl.ac.be](mailto:pardoen@imap.ucl.ac.be) (T. Pardoen).

## 1. Introduction

When combined with state of the art surface treatments, modern adhesives can exhibit very high toughness up to  $5 \text{ kJ/m}^2$  and good fatigue resistance even in harsh environments (e.g. Kinloch, 1997, 2002). Adhesive bonding has thus emerged as a serious candidate to replace rivets or welding in primary structural components. Its use in critical structural applications necessitates the development of robust integrity assessment methodologies. Indeed, design procedures for such critical applications are not solely based on strength but also on damage and fracture resistance. Although a consensus appears to have emerged about the testing methods and parameters to be employed to characterize bond toughness, numerous questions remain about the transfer of laboratory results to complex structures. The difficulty arises from the existence of constraint effects that affect the global bond toughness. Here we distinguish two types of constraint effects:

- *external constraint effects*: the state of deformation of the adherents affects the stress and strain distributions and hence the dissipation by irreversible deformation and damage within the adhesive layer (for instance, in a peel test, the measured bond toughness usually depends on the thickness of the peeling arm, see e.g. Wang et al., 2003);
- *internal constraint effects*: the thickness and width of the adhesive layer also affect the stress and strain distribution in the adhesive. For instance, a change of the adhesive layer thickness can cause a transition from small-scale yielding (SSY) conditions within the adhesive to fully plastic conditions (e.g. Kinloch and Shaw, 1981; Chai, 1995; Tvergaard and Hutchinson, 1994, 1996; Ikeda et al., 2000).

One-parameter fracture mechanics can obviously not predict constraint effects. Capturing constraint effects requires proper modelling of the mechanics of deformation in both the adherent and the adhesive.

An important step in this effort has been the introduction of cohesive zone models to describe the response of adhesive layers to mechanical loading and to simulate crack propagation (Yang et al., 1999; Yang and Thouless, 2001; Mohammed and Liechti, 2000; Sorensen, 2002; Ferracin et al., 2003). Fig. 1a represents the application of the cohesive zone model to the wedge opening test. This type of model considers only two constituents in the system: the adherents, which are modelled as elastic–plastic continua, and, the adhesive layer, with the mechanical response fully represented by the traction–opening response of the cohesive zone. Hence, in the present paper, this type of cohesive zone model will be called the ACZ model (for Adherents + Cohesive Zone). This modelling approach is very attractive because (i) cohesive zone models involve a limited number of parameters; (ii) mixed mode loading can easily be incorporated (Yang and Thouless, 2001; Kafkalidis and Thouless, 2002); and (iii) rate-dependent effects can be taken into account (e.g. Landis et al., 2000). Thouless and coworkers (e.g. Kafkalidis et al., 2000; Yang and Thouless, 2001) have proposed methods for identifying the cohesive zone response in

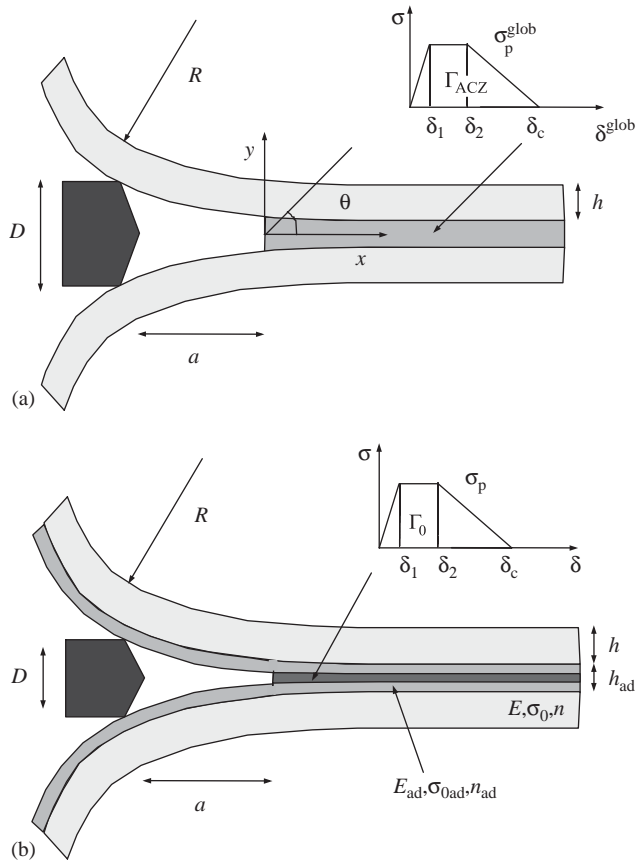


Fig. 1. Model for the plastic wedge-opened double-cantilever beam test; (a) “ACZ” description (Adherent + Cohesive Zone); (b) “AACZ” description (Adherent + Adhesive + Cohesive Zone).

the case of adhesive joints (see also [Andersson and Stigh, 2004](#)) and they have validated the method on a limited number of applications.

However, the use of a single cohesive zone to describe the entire response of an adhesive layer remains a strong simplification. Indeed, the mechanisms of cracking of an adhesive layer are very complex, involving multi-axial plastic deformation and various types of damage phenomena developing at different scales. A more versatile model is thus necessary in order to account for at least some of these mechanisms.

In this work, a model for the adhesive layer has been developed in the spirit of the works by [Tvergaard and Hutchinson \(1996\)](#), [Wei and Hutchinson \(1998\)](#), and [Madhusudhana and Narasimhan \(2002\)](#). This model is represented in [Fig. 1b](#). It will be called the AACZ model (for Adherent + Adhesive layer + Cohesive Zone). The model contains a finite thickness adhesive layer behaving as an elastic–plastic solid, in which a single row of cohesive zone elements representing the fracture process *within* the adhesive is embedded. The adherents are also elastic–plastic with strain

hardening. Then, the bond toughness  $\Gamma$  is defined as being equal to  $\Gamma_0 + \Gamma_p$ , where  $\Gamma_0$  is the intrinsic work of fracture associated with the embedded cohesive zone response and  $\Gamma_p$  is the contribution to the bond toughness arising from the plastic dissipation and stored elastic energy within the adhesive layer. In this study,  $\Gamma_0$  is taken as a material parameter independent of the local stress state. This assumption is important and will be discussed further at the end of the paper. Note however that a more general form of the model could also introduce a local stress state dependence of  $\Gamma_0$ . Our present assumption is made for the sake of simplifying the analysis by limiting the possible source of constraint effects. Then, changing the adhesive or adherent thickness induces constraint effects by affecting the plastic deformation in the adhesive layer, which translates into a change of  $\Gamma_p$ .

The aims of the paper are threefold:

- (1) To assess the AACZ model against experimental measurements involving “internal” and “external” constraint effects. The parameters of the AACZ model are identified from experiments on two different adhesives exhibiting very different fracture properties, which are representative of the behaviour of a wide range of different types of common adhesive systems. Most of the tests were performed using the wedge-peel test method using a variety of adherent and wedge thicknesses. Two other test geometries were also used.
- (2) To provide a rationale concerning constraint effects in the debonding of adhesive bonds in order to contribute to the development of transferable methods.
- (3) To better understand the meaning of the cohesive zone parameters in the ACZ model and to uncover the limitations of this model.

The experiments are described in the first section followed by selected results presented in Section 2. The model and numerical methods are presented in Section 3. The identification and validation of the model is presented in Section 4 with the results of a parametric study on adhesive and adherent thickness effects. The discussion in Section 5 focuses on elucidating the reasons for the constraint effects, on explaining the differences observed between the two adhesives, and on determining the limits of the ACZ model.

## 2. Experimental

### 2.1. Materials

Steel plates of thickness equal to either 0.78 or 1.2 mm were bonded on top of one another using structural adhesives. These steel adherents were tested in uniaxial tension and the stress strain curves were fitted using

$$\sigma = \begin{cases} E\varepsilon & (\sigma \leq \sigma_0), \\ \frac{\sigma_0}{(\sigma_0/E)^n} \varepsilon^n & (\sigma > \sigma_0), \end{cases} \quad (1)$$

where  $E$  is the Young's modulus (see Table 1),  $\sigma_0 = 150$  MPa for both thicknesses and  $n = 0.19$  and  $0.16$  for the  $0.78$  and  $1.2$  mm thicknesses, respectively.

Two different commercial epoxy-based adhesives were tested. The adhesive that will be designated as “yellow”, is a mono-component epoxy-based adhesive containing a large volume fraction of silicate particles to increase the stiffness. The adhesive that will be designated as “blue” is a mono-component epoxy adhesive with 70% epoxy resin diglycidyl ether of bisphenol-A incorporating 15% of rubbery particles and 5% of small silicate particles. The tensile properties of the adhesives are summarized in Table 1.

Under uniaxial tension, the yellow adhesive shows a brittle behaviour (elongation  $\leq 1\%$ ) with a Young's modulus  $E \approx 5$  GPa and a yield strength  $\sigma_0 \approx 30$  MPa. The measured strain rate sensitivity is very low for this material. The blue adhesive shows a ductile behaviour with an elongation  $\geq 5$ – $10\%$  under uniaxial tension with a Young's modulus  $E \approx 2$  GPa and a yield strength  $\sigma_0 \approx 35$  MPa at a strain rate of  $10^{-4} \text{ s}^{-1}$ . The behaviour of the adhesives in uniaxial tension is also described by Eq. (1). The strain rate sensitivity is moderate for this material. Note that strain rate effects will not be addressed in this paper.

The specimen geometry is shown in Fig. 2. The adhesives were deposited on steel plates between two Teflon tapes separated by 80 mm. For preparing samples with different bond thicknesses, the adhesive thickness was controlled by spacers (Fig. 2a) located near the beginning and near the end of the adhesive layer or by uniformly spreading metallic wires (Fig. 2b) or glass beads of diameter equal to the desired thickness (Fig. 2c). The three methods lead to similar fracture toughness results.

## 2.2. The plastic wedge peel test

The plastic wedge peel test has received attention in the recent literature (Thouless et al., 1998; Kafkalidis et al., 2000; Ferracin et al., 2003). In this test, two bonded metal plates are separated by means of a wedge inserted at constant speed along the interface (Fig. 3). The wedge induces a constant opening rate of the two plates, leading, after an initiation stage, to a steady-state crack length  $a$ . The test is designed in such a way as to induce plastic bending of the adherents during the failure of the

Table 1  
Elastic and plastic properties of the adhesives and adherents measured experimentally by tension testing

Materials	Young's modulus $E$ (GPa)	Poisson ratio $\nu$	Yield strength $\sigma_0$ (MPa)	Strain hardening exponent $n$
Yellow adhesive	5	0.45	30	(0.1)
Blue adhesive	2	0.45	35	(0.1)
0.78 mm steel adherent	206	0.3	150	0.19
1.2 mm steel adherent	206	0.3	150	0.16
Al alloy for TDCB	70	0.35		

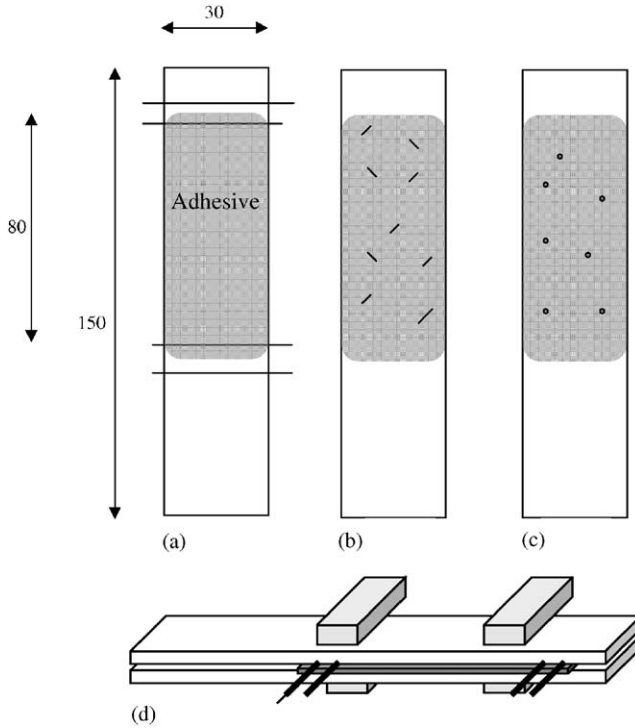


Fig. 2. Preparation and geometry of the adhesive joints to be used with the wedge peel test (dimensions in mm); thickness is controlled by (a) parallel metallic wires, or (b) a dispersion of short metallic wires, or (c) a dispersion of glass beads; (d) full sandwich specimen subjected to dead loads during curing.

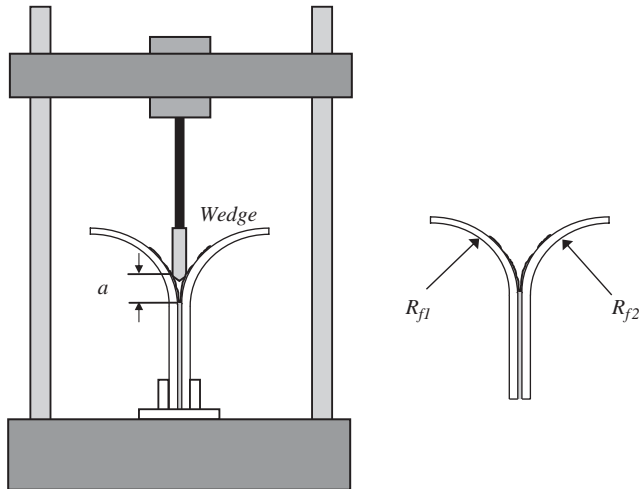


Fig. 3. Plastic wedge peel test method and definition of the crack length  $a$  measured during the test and radii of curvature  $R_{f1}$  and  $R_{f2}$  measured after testing.

adhesive bond (in contrast to the more classical elastic wedge test). Using the plastic wedge peel test, the joint toughness can be approximately inferred from the radius of curvature of the adherents and/or the crack length using either analytical solutions or an inverse identification procedure based on a cohesive zone representation (Yang et al., 1999; Ferracin et al., 2003). The identification procedure used in the present paper will be discussed in Section 4.

The tests were performed by driving the wedge between the two adherents at a speed of 10 mm/min using a universal testing machine. The wedge thickness was usually equal to 1.8 mm but a few tests were also performed with a 4 mm thick wedge. A CDD camera was used for measuring the crack length  $a$ , defined as the distance between the crack tip and the point of contact of the wedge with the adherent. After completion of the test, the radii of curvature of the two plastically deformed plates were obtained by measuring the co-ordinates of a discrete number of points along the curved adherent using a profile projector and by fitting these co-ordinates by the equation of a circle. Steady-state debonding was observed during the main part of the test, i.e. constant radii of curvature of the adherents and constant crack length. The radii of curvature of the two adherents were never perfectly equal. A representative radius of curvature was defined as (see Thouless et al., 1998)

$$R_f = \left( \frac{1}{R_{f1}^{n+1}} + \frac{1}{R_{f2}^{n+1}} \right)^{-1/2(n+1)}, \quad (2)$$

where  $R_{f1}$  and  $R_{f2}$  are the two measured radii of curvature and  $n$  is the strain hardening exponent of the adherents. At least five specimens were tested for each combination of experimental conditions. For each specimen, at least five measurements of the crack length  $a$  were made during the test and the values presented in Section 4.1 are the averages and standard deviations of all measurements for one combination of testing condition. For a few specimens, the test was stopped before complete delamination and ink was injected at the crack front. The specimens peeled afterwards revealed a straight crack front.

### 2.3. Other fracture tests

The plane strain fracture toughness of the bulk blue adhesive was measured using the compact tension (CT) procedure as described by the ASTM standards E561, E813 and E399. This procedure has been widely used for measuring the fracture toughness of modified epoxies (e.g. Ochi et al., 2000; Ochi and Shimaoka, 1999; Lowe et al., 1996). The dimensions of the specimens are given in Fig. 4. This piece was prepared by injection of the adhesive in an aluminium mould followed by curing for 1 h at 170 °C. A sharp pre-crack was formed using a razor blade. The tests were made on a universal testing machine at a speed of 0.2 mm/min. A properly calibrated clip-on device was placed at the mouth of the specimen for measuring the crack mouth opening  $u$ . During testing,  $u$  was continuously recorded together with the load

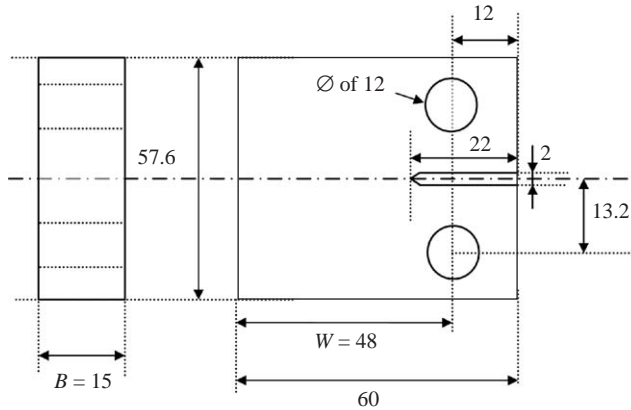


Fig. 4. Compact tension (CT) geometry for bulk properties measurement (dimensions in mm).

*P*. Unloadings were performed following standard procedures at regular intervals during crack extension in order to evaluate the compliance, and hence the crack length. Denoting  $J_e$  and  $J_p$  the elastic and plastic components of the  $J$ -integral evaluated during each unloading sequence, the measured value of the  $J$ -integral was taken as

$$J = J_e + J_p \tag{3}$$

with

$$J_e = \frac{K^2(1 - \nu^2)}{E} = \left( \frac{P}{B\sqrt{W}} f(a/W) \right)^2 \frac{(1 - \nu^2)}{E} \tag{4}$$

and

$$J_p = \frac{\eta A}{B(a_0 - a)}, \tag{5}$$

where  $E$  and  $\nu$  are the Young’s modulus and Poisson’s ratio of the epoxy, respectively,  $P$  is the load,  $B$  and  $W$  are two dimensions of the specimen indicated in Fig. 4,  $a$  is the crack length,  $a_0$  is the initial crack length,  $f(a/W)$  is a geometrical factor,  $\eta$  is equal to  $2 + 0.522(a - a_0)/W$  and  $A$  is the area under the load–displacement curve. The plane strain fracture toughness at cracking initiation was evaluated from the  $J - \Delta a$  curve as the intercept with the blunting line. The fracture toughness at cracking initiation is the only information from these fracture tests that will be used for the analysis later in the paper.

For the blue adhesive, a few tests were also performed using the Tapered Double Cantilever Beam (TDCB) geometry, see Fig. 5, following the recommendations given in the ESIS protocol TC4 (Blackman and Kinloch, 1997). In order to provide an energy release rate that, as a first approximation, is independent of the crack length  $a$ , the variation of the height  $h$  of the adherent arms is designed to

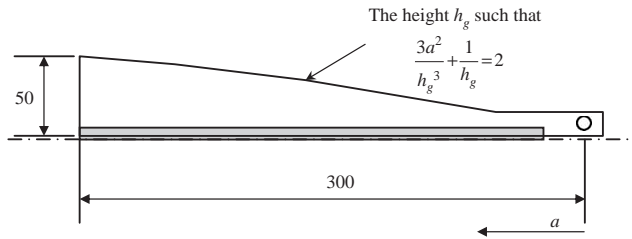


Fig. 5. The Tapered Double Cantilever Beam (TDCB) geometry (dimensions in mm).

comply with the relation

$$\frac{3a^2}{h^3} + \frac{1}{h} = m, \tag{6}$$

where  $m$  is a constant. After bonding the adherents, the adhesive was cured for 45 min at 170 °C. The aluminium arms had been previously etched by chromic acid to ensure good adhesion and a crack path contained within the adhesive layer. Testing was performed with an opening speed of 0.1 mm/min. The load and displacements were recorded during testing and the crack length was measured multiple times during propagation. As proposed by Blackman and Kinloch (1997), the mode I fracture toughness  $G_{Ic}$  for the TDCB geometry was evaluated using a model taking into account the “root rotation” of the beam:

$$G_{Ic} = \frac{4P^2}{E_s B^2} m \left( 1 + 0.43 \left( \frac{3}{ma} \right)^{1/3} \right), \tag{7}$$

where  $P$  is the load at fracture,  $B$  is the specimen width,  $E_s$  is the Young’s modulus of the adherent and  $m$  was always equal to 2 mm<sup>-1</sup>. The TDCB specimen arms were made of an age-hardened aluminium alloy with a Young’s modulus  $E_{Al} = 70$  GPa.

### 3. Models and numerical methods

#### 3.1. The AACZ model

Both the adherents and the adhesive were modelled using rate-independent isotropic linear elasticity (with Young’s moduli  $E$  and  $E_{ad}$  and Poisson’s ratios  $\nu$  and  $\nu_{ad}$ ) and the isotropic  $J_2$  flow plasticity theory. For both materials, the stress–strain response was represented by Eq. (1), hence involving a yield strength  $\sigma_{0ad}$  and a hardening exponent  $n_{ad}$  for the adhesive layer.

Following the approach promoted by Tvergaard and Hutchinson (1992, 1994) and applied later by several authors (e.g. Madhusudhana and Narasimhan, 2002), the fracture process within the adhesive layer is simulated using an interface traction–separation law (relating the normal stress  $\sigma$  to the opening displacement  $\delta$ ) characterized by the adhesive fracture energy, denoted  $\Gamma_0$ , and a peak stress,

denoted  $\sigma_p$  (see Fig. 1b). This type of traction–separation law with the form depicted in Fig. 1 was proposed by Tvergaard and Hutchinson (1992). The shape parameters  $\lambda_1 = \delta_1/\delta_c$  and  $\lambda_2 = \delta_2/\delta_c$  are kept constant for all calculations presented here, equal to 0.15 and 0.5, respectively. Note that once the maximum separation  $\delta_c$ , the peak stress  $\sigma_p$ , and the shape parameters  $\lambda_1$  and  $\lambda_2$  are set,  $\Gamma_0$  can be obtained from

$$\Gamma_0 = \frac{\sigma_p \delta_c}{2} (1 - \lambda_1 + \lambda_2). \tag{8}$$

The three lengths entering the model are the wedge thickness  $D$ , the adherent thickness  $h$  and the adhesive layer thickness  $h_{ad}$ . The outputs of the model, which will be compared to experiments, are the final radius of curvature of the arms  $R$  and the crack length  $a$ . Dimensional analysis dictates that

$$\begin{aligned} \frac{R}{h} &= F_1 \left\{ \underbrace{\frac{\sigma_0}{E}, n, \nu, \frac{\sigma_{0ad}}{E_{ad}}, n_{ad}, \nu_{ad}, \frac{\sigma_0}{\sigma_{0ad}}}_{\text{elasto-plastic properties of adherent and adhesive}}, \underbrace{\frac{\Gamma_0}{\sigma_{0ad} h_{ad}}, \frac{\sigma_p}{\sigma_{0ad}}, \lambda_1, \lambda_2}_{\text{fracture properties of adhesive}}, \underbrace{\frac{D}{h}, \frac{h}{h_{ad}}}_{\text{geometry}} \right\}, \\ \frac{a}{h} &= F_2 \left\{ \frac{\sigma_0}{E}, n, \nu, \frac{\sigma_{0ad}}{E_{ad}}, n_{ad}, \nu_{ad}, \frac{\sigma_0}{\sigma_{0ad}}, \frac{\Gamma_0}{\sigma_{0ad} h_{ad}}, \frac{\sigma_p}{\sigma_{0ad}}, \lambda_1, \lambda_2, \frac{D}{h}, \frac{h}{h_{ad}} \right\}. \end{aligned} \tag{9}$$

Other important outputs from the computations are the plastic dissipation (plus some elastic stored energy) in the adhesive layer,  $\Gamma_p$ , which will be used to evaluate the overall bond toughness  $\Gamma = \Gamma_0 + \Gamma_p$ , and the plastic zone sizes and shapes.

### 3.2. The ACZ model

The ACZ model is similar to the AACZ model except that the deformation and the fracture of the adhesive are lumped together, i.e. the traction separation law is taken to represent the response of the entire adhesive layer. The peak stress is then denoted  $\sigma_{pglob}$  and the global bond toughness enclosed into the traction separation law is denoted  $\Gamma_{ACZ}$ . The critical displacement is the sum of the CTOD at the tip of the debond crack and the total elongation inside the adhesive layer. For this model, dimensional analysis yields

$$\begin{aligned} \frac{R}{h} &= F_3 \left\{ \underbrace{\frac{\sigma_0}{E}, n, \nu}_{\text{elasto-plastic properties of adherent}}, \underbrace{\frac{\Gamma_{ACZ}}{\sigma_0 h}, \frac{\sigma_{pglob}}{\sigma_0}, \lambda_1, \lambda_2}_{\text{fracture and flow properties of adhesive}}, \underbrace{\frac{D}{h}}_{\text{geometry}} \right\}, \\ \frac{a}{h} &= F_4 \left\{ \frac{\sigma_0}{E}, n, \nu, \frac{\Gamma_{ACZ}}{\sigma_0 h}, \frac{\sigma_{pglob}}{\sigma_0}, \lambda_1, \lambda_2, \frac{D}{h} \right\}. \end{aligned} \tag{10}$$

A comprehensive parametric study of the relationship between the global bond toughness and the radius of curvature (and crack length) computed using the ACZ model as been given by Ferracin et al. (2003).

### 3.3. Numerical methods

A steady-state finite element formulation for small strain–small rotation crack propagation problems was first applied by Dean and Hutchinson (1980) and later used by several other authors for different problems (e.g. Wei and Hutchinson, 1998). The formulation consists of finding an equilibrium solution for the displacements based on a previous approximate distribution of plastic strains and then integrating the plasticity laws along streamlines to determine new approximations for stresses and plastic strains. This procedure is repeated until convergence is achieved. The wedge peel test problem requires, at a minimum, a small strain–large rotation formulation. The variational principle for this formulation is written as

$$\int_V \sigma_{ij} \delta \varepsilon_{ij} \, dV = \int_S t_i \delta u_i \, dS. \tag{11}$$

where  $V$  is the volume of the body in the undeformed configuration,  $S$  is its surface,  $\sigma_{ij}$  is the second Piola–Kirchhoff stress,  $t_i$  is the traction applied to the boundary,  $u_i$  is the total displacement, and  $\varepsilon_{ij}$  is the Green–Lagrange strain tensor given in terms of displacement gradients as

$$\varepsilon_{ij} = \frac{1}{2}(u_{i,j} + u_{j,i} + u_{k,i}u_{k,j}). \tag{12}$$

The iterative procedure used to solve for the distribution of plastic strain is based on Eq. (11), and assumes *small strains* such that  $\varepsilon_{ij}$  can be additively decomposed into elastic and plastic parts. Then, the second Piola–Kirchhoff stress is given as

$$\sigma_{ij} = C_{ijkl}(\varepsilon_{kl} - \varepsilon_{kl}^p), \tag{13}$$

where  $C_{ijkl}$  is the elastic stiffness tensor, which can be written in terms of  $E$  and  $\nu$ , and  $\varepsilon_{ij}^p$  is the plastic part of the strain. Note that finite rotations are still allowed. The plastic strains are determined by  $J_2$  flow theory. Within a spherical yield surface given by  $3s_{ij}s_{ij}/2 - \sigma_0^2 = 0$ , the increments of plastic strain are zero. When the stress state is on the yield surface and the load increment is directed outward from the surface, plastic strain rates express as

$$\dot{\varepsilon}_{ij}^p = \frac{3}{2} \dot{\varepsilon}^p \frac{s_{ij}}{\bar{\sigma}} \tag{14}$$

where  $s_{ij}$  is the deviatoric part of  $\sigma_{ij}$ ,  $\bar{\sigma} = \sqrt{3s_{ij}s_{ij}/2}$  is the effective stress, and  $\dot{\varepsilon}^p = \sqrt{2\dot{\varepsilon}_{ij}^p\dot{\varepsilon}_{ij}^p}/3$  is the effective plastic strain increment. A power-law hardening rule derived from Eq. (1) is used to relate the effective stress to the effective plastic strain as

$$\left(\frac{\bar{\sigma}}{\sigma_0}\right)^{1/n} - \frac{\bar{\sigma}}{\sigma_0} = \frac{E\bar{\varepsilon}^p}{\sigma_0}, \tag{15}$$

where  $n$  is the hardening exponent,  $\sigma_0$  is the initial yield strength of the material, and  $\bar{\varepsilon}^p = \int \dot{\varepsilon}^p \, dt$  is the accumulated effective plastic strain.

The iterative procedure used to determine the distribution of plastic strains is analogous to that used for the linear kinematics formulation and is written as

$$\int_V \delta \varepsilon_{ij} C_{ijkl} \varepsilon_{kl}^{n+1} dV + \int_{S_c} \delta u_1 \kappa^{n+1} \delta dS = \int_V \delta \varepsilon_{ij} C_{ijkl} \varepsilon_{kl}^p dV + \int_{S_c} \delta u_1 \kappa^n \delta^p dS + \int_S t_i \delta u_i dS. \quad (16)$$

Here,  ${}^{n+1}\varepsilon_{ij}$  and  ${}^{n+1}\delta$  are the strain and crack opening displacement computed at the  $n + 1$ th iteration,  ${}^n\varepsilon_{ij}^p$  and  ${}^n\delta^p$  are the plastic strain and plastic part of the crack opening displacement computed at the  $n$ th iteration, and  $\kappa$  is the initial slope of the traction separation curve. Then,  $V$  is the volume of the material in the reference configuration,  $S_c$  is the cohesive surface ahead of the crack tip, and  $S$  is the external surface in the reference configuration where tractions or displacements are applied. The integrals on the left side of Eq. (16) form the stiffness matrix and vector of unknown displacements at the  $n + 1$ th iteration. The surface integrals over  $S_c$  account for the cohesive tractions ahead of the crack tip. The volume integral on the right-hand side can be interpreted as a body force due to plastic strains. In order to alleviate convergence problems associated with the cohesive zone elements, an optimal lumping procedure was used to perform the cohesive surface integrations.

The solution procedure is described as follows. During a given plasticity iteration of the procedure the plastic strains are known from the previous iteration and *fixed*. Eq. (16) then defines a set of non-linear finite element equations that must be solved with a Newton–Raphson method. Let us call any Newton–Raphson step an equilibrium iteration. Note that during the equilibrium iterations the plastic strain distributions do not change. Once the equilibrium iterations have converged to a solution for the given distribution of plastic strains, a new plastic strain distribution is approximated by integrating the plasticity law, Eq. (14), along streamlines defined by a constant distance above or below the crack plane. This represents a previously mentioned plasticity iteration. Hence, for each plasticity iteration there are multiple equilibrium iterations. Then, the entire computation is complete when the distributions of plastic strains converge. In a steady-state formulation, most geometrical parameters such as the crack length  $a$  can be imposed. The crack tip will effectively be located where it has been fixed if the crack tip opening displacement (CTOD) at this point is equal to the maximum separation of the cohesive zone  $\delta_c$ .

Since the wedge-peel test is symmetric, only half of the sandwich needs to be analyzed. Plane strain conditions are assumed since the width of the adherent is much larger than its thickness. The crack is assumed to have propagated a sufficient distance such that steady-state conditions prevail for the entire structure. The wedge is modelled with a fixed displacement boundary condition perpendicular to the crack plane of magnitude  $D$ , the wedge thickness. Eight-noded isoparametric elements are implemented and the relevant boundary conditions have been imposed upstream from the crack tip in order to fix all rigid body displacements.

An extensive mesh convergence analysis was carried out. The mesh was particularly refined at the point of contact of the wedge and at the crack tip. The mesh convergence analysis was found to be crucial in the case of the AACZ model in order to guarantee that the plasticity within the adhesive layer is accurately captured while having enough elements to also represent the fracture process.

The plastic dissipation  $\Gamma_p$  (plus any locked-in elastic energy) in the adhesive layer is computed by integrating the work density far downstream along the bond layer thickness (this is an exact statement within the context of a steady-state problem as analyzed here):

$$\Gamma_p = 2 \int_0^{h_{ad}/2} W dy \text{ (per unit of beam width)} \quad (17)$$

with

$$W = \int_0^{\varepsilon_{ij}} \sigma_{ij} d\varepsilon_{ij}. \quad (18)$$

### 3.4. Small-scale yielding (SSY) formulation

The same numerical procedures were applied to simulate the limiting case of a very long and thick (elastic) adherent. This situation is modelled as two semi-infinite half-spaces bonded together by an adhesive layer of thickness  $h_{ad}$ . The boundary conditions are now displacements applied along the outer boundary of the effectively infinite adherents based on the asymptotic mode I  $K$ -field displacements using the elastic properties of the adherents (there is no wedge for this case). In these simulations, the total bond toughness

$$\Gamma = \frac{K^2}{E} (1 - \nu^2) \text{ (} E \text{ and } \nu \text{ are the properties of the adherents)} \quad (19)$$

is imposed by controlling the applied  $K$ -field. The simulations are repeated with different values of  $K$  until the CTOD in the adhesive is equal to the maximum separation of the cohesive zone  $\delta_c$ . A method used to check the convergence was to verify that the applied  $\Gamma$  is equal  $\Gamma_0 + \Gamma_p$ , where  $\Gamma_p$  was calculated as explained above, Eqs. (17) and (18). This SSY formulation was also used to model the TDCB specimens.

## 4. Results: Experiments, identification and validation of the model, parametric study

### 4.1. Test results

Table 2 presents the values of the average radius of curvature  $R$  and crack length  $a$  measured for both adhesives for different bond thicknesses. Fig. 6 gathers the results in graphical form. The effect of the adhesive thickness is larger for the yellow adhesive than for the blue adhesive. The corresponding values for bond toughness are also indicated but their identification is explained in Section 4. Table 3 presents the results for the TDCB and CT tests carried out for the blue adhesive.

Table 2

Experimental radius of curvature, crack length and bond toughness for the two adhesives for various adhesive layer thicknesses, adherent thicknesses, and wedge thicknesses

Adhesive $h_{\text{ad}}$	Specimen and test configurat.	Adherent thickness (mm) $h$	Adhesive layer thickness (mm)	$R_{\text{exp}}$ (mm)	$a_{\text{exp}}$ (mm)	$R_{\text{model}}$ (mm)	$a_{\text{model}}$ (mm)	$\Gamma_{\text{model}}$ (J/m <sup>2</sup> )
Blue	Wedge $D = 1.8$ mm	1.2	0.05	$27.4 \pm 1.5$	$5.62 \pm 0.2$	19	4.8	3600
Blue	Wedge $D = 1.8$ mm	1.2	0.18	$18.4 \pm 0.3$	$4.82 \pm 0.15$	18.5	4.78	3750
Blue	Wedge $D = 1.8$ mm	1.2	0.89	$21.5 \pm 2.0$	$4.88 \pm 0.1$	20.7	4.95	5725
Blue	Wedge $D = 1.8$ mm	0.78	0.18	$9.37 \pm 0.67$	Not measured	11	3.6	3825
Blue	Wedge $D = 4$ mm	1.2	0.18	$13.8 \pm 1.6$	Not measured	15.2	7.3	3800
Blue	Wedge $D = 4$ mm	0.78	0.18	$7.03 \pm 0.56$	Not measured	8.7	5.3	3900
Yellow	Wedge $D = 1.8$ mm	0.78	0.08	$185 \pm 15$	$11.3 \pm 0.8$	188	14.2	200
Yellow	Wedge $D = 1.8$ mm	0.78	0.24	$109 \pm 4$	$10.4 \pm 0.3$	107	11.3	275
Yellow	Wedge $D = 1.8$ mm	0.78	0.82	$99 \pm 23$	$10.8 \pm 0.4$	126	11.9	425

The values of the radius of curvature and crack length predicted by the model are obtained using, for the yellow adhesive,  $\sigma_p = 3.34\sigma_{\text{padhesive}} = 100$  MPa and  $\Gamma_0 = 175$  J/m<sup>2</sup> and, for the blue adhesive,  $\sigma_p = 3.25\sigma_{\text{padhesive}} = 114$  MPa and  $\Gamma_0 = 3500$  J/m<sup>2</sup>.

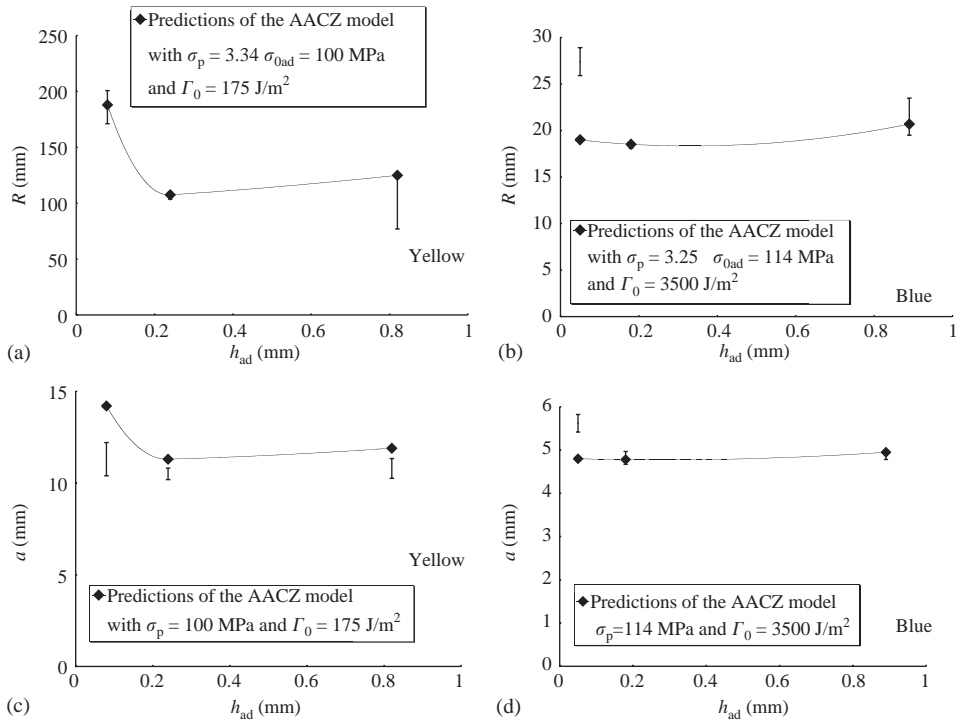


Fig. 6. Comparison of the measured (□) and predicted (◆) values of the radius of curvature (a and b) and crack lengths (c and d) for the two adhesives (yellow: (a and c); blue: (b and d)) and different adhesive layer thicknesses.

Table 3  
Results for the TDCB and CT tests carried out for the blue adhesive

Adhesive	Specimen and test configuration	Bond thickness (mm)	$\Gamma_{exp}$ (J/m <sup>2</sup> )	$\Gamma_{model}$ (J/m <sup>2</sup> )
Blue	CT	NA	3200 (at cracking initiation) Eq. (8)	NA
Blue	TDCB	0.89	6100 Eqs. (4)–(6)	4200 (SSY value)

Although the comparison of the radii of curvature or crack lengths is only appropriate if exactly the same adherent thicknesses are used, one can certainly anticipate from these results that the blue adhesive has a much larger fracture resistance than the yellow adhesive (see Ferracin et al., 2003, for a detailed analysis of the relationship between curvature and bond toughness).<sup>1</sup>

<sup>1</sup>The difference would be even larger if the adherents had the same thickness, as the radius of curvature tends to decrease with increasing adherent thickness.

The effect of the adhesive layer thickness on the radius of curvature is obvious for the yellow adhesive. For the blue adhesive, the radius of curvature is smaller for the thin adhesive layer thickness but remains constant for the thicker layers.

As the test results are very different for the two adhesives, the fracture surfaces obtained after the tests were investigated by scanning electron microscopy (SEM) in order to reveal the differences in the crack extension mechanisms. This type of study is distinct from the core objective of this paper, and hence the interested reader is referred to Appendix A for more details.

#### 4.2. Identification of the fracture parameters

The properties of the adhesives and adherents were given in Section 2. The hardening exponent of both the yellow and blue adhesives was arbitrarily chosen equal to 0.1.<sup>2</sup> The peak stress  $\sigma_p$  and fracture energy  $\Gamma_0$  were identified based on the experimental values of the radius of curvature  $R$  corresponding to two different adhesive thicknesses (for the blue adhesive: lines 2 and 3 in Table 2; for the yellow adhesive: lines 7 and 8 in Table 2). This procedure was preferred over an identification based on both the crack length and radius of curvature, as the measurement of the crack length is much less accurate due to uncertainties associated with the precise location of the crack tip. Several simulations with different values of  $\sigma_p$  and  $\Gamma_0$  are performed for the two specimens (differing only by the adhesive layer thickness) until a very close match is found between the predictions and the experimental data. The results are as follows:

For the yellow adhesive :  $\sigma_p = 3.34\sigma_{0ad} = 100 \text{ MPa}$  and  $\Gamma_0 = 175 \text{ J/m}^2$ .

For the blue adhesive :  $\sigma_p = 3.25\sigma_{0ad} = 114 \text{ MPa}$  and  $\Gamma_0 = 3500 \text{ J/m}^2$ .

Note also that peak stresses larger than 3 times the adhesive yield strength are physically realistic (values larger than 3 are required to generate significant plasticity in the joint, see Tvergaard and Hutchinson, 1996).

#### 4.3. Validation of the model

In the case of the blue adhesive, the identified bond toughness  $\Gamma_0$  agrees with the fracture toughness measured on bulk CT samples:  $G_{Ic} = 3200 \text{ J/m}^2$  (even though, as shown in Appendix A, it is not clear that the fracture mechanisms are exactly the same). Based on the assumption that  $\Gamma_0$  is a constant, thus independent of the crack advance, these two quantities must be equivalent. This is a classical fracture mechanics statement which can be demonstrated by reducing the contour used for

<sup>2</sup>The adhesive materials tested in this work do show a large strain hardening capacity at low plastic strain (<1%). In the yellow adhesive, the adhesive material rapidly fails after the onset of yielding. In the blue adhesive, the hardening capacity decreases to almost 0 for strain around 3–5%. The strain hardening exponent is thus far from constant. A strain hardening exponent of 0.1 is a good compromise considering that the typical plastic strains occurring in the plastic zones typically range between 1% and 5%.

calculating the  $J$  integral to the boundary of the fracture process zone described here by a cohesive law (Tvergaard and Hutchinson, 1992).

The model can be further validated by comparing its predictions to test results for other specimens with different adhesive layer thickness and adherent thickness, or for different testing configurations (TDCB or other wedge thicknesses).

#### 4.3.1. Capturing the effect of the adhesive layer thickness

In Figs. 6(a–d), the predictive potential of the model is assessed through the comparison of experimental and modelling results for the adhesive thickness not used in the identification process and by comparing the measured and predicted crack lengths.

The agreement for the yellow adhesive is good except that the predicted crack length systematically overestimates the measured one. It should be noted that the crack length measurements are always lower bound values as it is never possible to detect the exact location of the crack tip (especially in the yellow adhesive which shows very small CTODs). Obviously, the discrepancy can also result from the approximations involved in the model (see Section 5).

In the case of the blue adhesive, the use of a single set of  $\Gamma_0$  and  $\sigma_p$  values did not allow for the prediction of the low overall bond toughness (i.e. the large value of  $R$ ) measured for the smallest thickness (50  $\mu\text{m}$ ). Two reasons are proposed for this behaviour. First, the fracture surface observations presented in Appendix A revealed that the length scale of the fracture mechanisms is in the order of a 100–200  $\mu\text{m}$  in the thicker adhesive layers, which means that, in the thin adhesive layer, these *intrinsic* fracture mechanisms are constrained by the thickness of the layer and cannot fully develop. This geometric constraint effect on the fracture process zone extension will be discussed in Section 5.4. Secondly, fracture occurs in the middle of the adhesive layer when the adhesive layer is thin and near the interface when the adhesive layer is thicker. The position of the crack path in the layer affects the plastic strain distribution and magnitude, and therefore the contribution due to the plastic yielding in the adhesive layer. This feature of the crack path asymmetry has not yet been modelled. For the other two adhesive layer thicknesses (0.18 and 0.89 mm), the predicted crack lengths are in excellent agreement with the measurements.

Let us now consider the variation of the predicted bond toughness values as a function of adhesive layer thickness and adhesive type. These values are compared to test results in Table 2 and they are presented in Fig. 7, which also includes calculations for other adhesive layer thicknesses outside the range tested experimentally. Starting from a thickness close to zero, an increase of adhesive layer thickness induces a drastic increase of the bond toughness, especially for the yellow system. This effect results only from the increase of  $\Gamma_p$  and can thus be captured only if plasticity within the adhesive is explicitly taken into account in the model. Fig. 7 shows that, at some thickness, the bond toughness reaches a maximum and then decreases to a constant value as the adhesive layer thickness increases. This evolution will be discussed in more detail in Section 5.

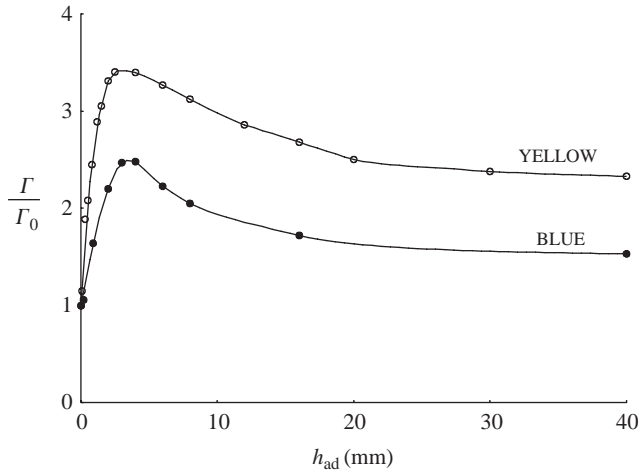


Fig. 7. Variation of the ratio  $\Gamma/\Gamma_0$  as a function of the adhesive layer thickness for the yellow and blue adhesives. The thickness of the adherent is equal to 0.78 mm for the yellow adhesive and 1.2 mm for the blue adhesive. The wedge thickness is equal to 1.8 mm.

#### 4.3.2. Capturing the adherent and wedge thickness effects

For the blue adhesive, debonding was also simulated using  $\sigma_p = 3.25 \sigma_{0ad} = 114 \text{ MPa}$  and  $\Gamma_0 = 3500 \text{ J/m}^2$  for assemblies made with thin adherents (0.78 mm) and for tests carried out with another wedge thickness (4 mm) (see Table 2). The results are given in Table 2. The agreement with the experiments is quite satisfactory.

#### 4.3.3. Capturing a change of specimen configuration

The bond toughness predicted using the SSY model with  $h_{ad} = 0.89 \text{ mm}$  is equal to  $4200 \text{ J/m}^2$ . This value is significantly larger than the value of  $\Gamma_0 = 3500 \text{ J/m}^2$  identified previously, but it remains much smaller than the experimental value extracted from the TDCB samples using Eqs. (3)–(5), which was equal to  $6100 \text{ J/m}^2$ . The most sensible origin for this discrepancy is that the fracture is cohesive in the middle of the bond for the TDCB whereas the values of  $\sigma_p$  and  $\Gamma_0$  have been identified for a cohesive-near-the-interface mode of crack propagation in the case of the wedge peel tests. This point is addressed in Section 5.4.

#### 4.4. Parametric study about the effect of the adhesive and adherent thickness

Fig. 8 shows the variation of the bond toughness  $\Gamma/\Gamma_0$  as a function of the adhesive layer thickness for various adherent thicknesses as well as for the limit case of an infinite adherent subjected to the  $K$ -field boundary conditions. The adhesive has the properties of the yellow system while the adherents have the properties of the 0.78 mm steel plates. The results for the 0.78 mm adherent are thus similar to the ones shown in Fig. 7. The results obtained for other adherent thicknesses have not

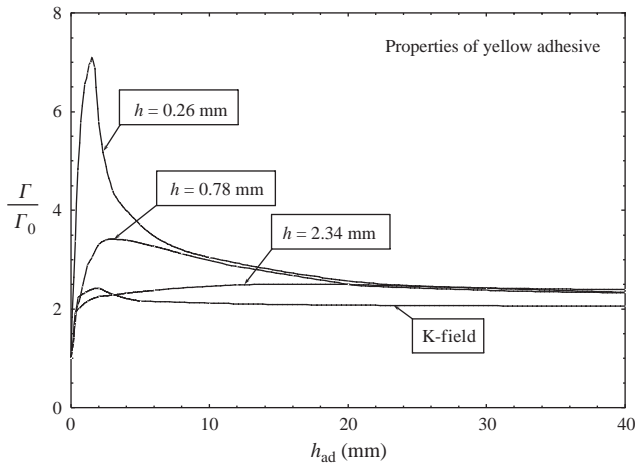


Fig. 8. Variation of the bond toughness as a function of the adhesive line thickness for different adherent thicknesses using the properties of the yellow system.

been compared with experiments. These results show that the total bond toughness not only depends on the adhesive layer thickness but is also significantly affected by the adherent thickness. The effect of the adhesive layer thickness is very distinct for thin adherents: the bond toughness  $\Gamma$  can be several times larger than the work of separation  $\Gamma_0$ . The results obtained for a thick adherent are similar to the results obtained for the  $K$ -field system. Only for a very thick (unrealistic in the practice) adhesive layer thickness does the bond toughness become independent of the adherent thickness.

Fig. 9 shows the variation of the plastic zone height as a function of the adhesive layer thickness for various adherent thicknesses, as well as for the limit case of an infinite adherent subjected to the  $K$ -field boundary conditions. The evolution of the plastic zone height indicates the origin of the variation of the bond toughness shown in Fig. 8. The large values of  $\Gamma$  obtained for thin adherents at intermediate bond thickness are directly related to the larger plastic zone sizes, which in most cases implies a larger  $\Gamma_p$ . Note however that it is not only the size of the plastic zone but also the magnitude of the plastic strains that affect  $\Gamma_p$ . The range of adhesive layer thickness for which full through-thickness yielding (i.e. a fully plastic adhesive layer) is observed depends on the adherent thickness. Finally, at very large adhesive thickness, the plastic zone becomes independent of specimen dimensions.

#### 4.5. Identification of the parameters for the ACZ model

The parameters  $\sigma_{p\text{glob}}$  and the bond toughness  $\Gamma_{\text{ACZ}}/\Gamma_0$  of the ACZ model have been identified in order to reproduce the values of  $R$  and  $a$  predicted by the AACZ

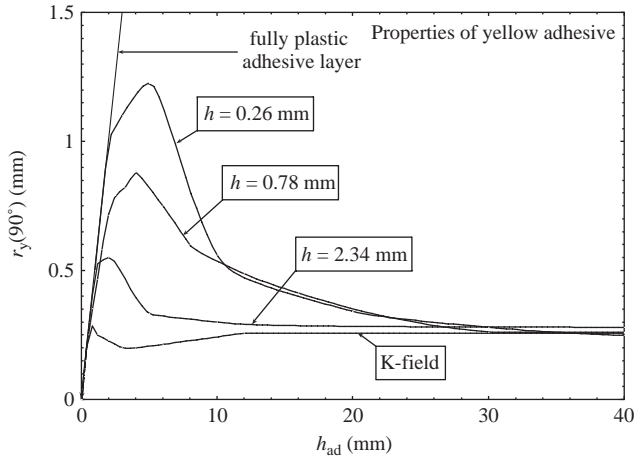


Fig. 9. Variation of the plastic zone height as a function of the bond line thickness for different adherent thicknesses using the properties of the yellow system.

model for each adhesive and each bond thickness. This identification procedure requires multiple simulations of the wedge peel test using the ACZ model with various sets of  $\sigma_{\text{pglob}} - \Gamma_{\text{ACZ}}$  (see Ferracin et al., 2003, for a detailed description of the identification procedure associated with the use of the ACZ model). Fig. 10 presents the variation of  $\Gamma_{\text{ACZ}}/\Gamma_0$  and of  $\sigma_{\text{pglob}}/\sigma_p$  with the bond thickness for the conditions tested experimentally. In this range of parameters, the ratio  $\Gamma_{\text{ACZ}}/\Gamma_0$  matches the evolution of  $\Gamma/\Gamma_0$  (see Fig. 7). The global peak stress decreases with increasing adhesive layer thickness. The effect is very pronounced for the yellow adhesive, in which the peak stress at intermediate and large thicknesses is significantly lower than the intrinsic strength of the adhesive. For the blue adhesive, the global peak stress is close to  $\sigma_p$ , i.e. the “intrinsic strength” or local adhesive peak stress.

## 5. Discussion and conclusions

The literature provides many examples of a dependence of bond toughness on adhesive layer thickness (e.g. Bascom et al., 1975; Kinloch and Shaw, 1981; Chai, 1986, 1995; Daghyani et al., 1995; Ikeda et al., 2000), on test configuration, or on adherent thickness (e.g. Sener, 1998; Ikeda et al., 2000; Wang et al., 2003). The aim of this discussion is to address the problem of transferability of bond toughness measurements in the case of mode I loading conditions, allowing for changes in the geometrical parameters and loading configuration, from the point of view that only the plasticity in the adhesive is responsible for the constraint effects. The other possible source of constraint effect is through a dependence of  $\Gamma_0$  and  $\sigma_p$  on the stress state. This last type of effect, on the local stress state dependence of the

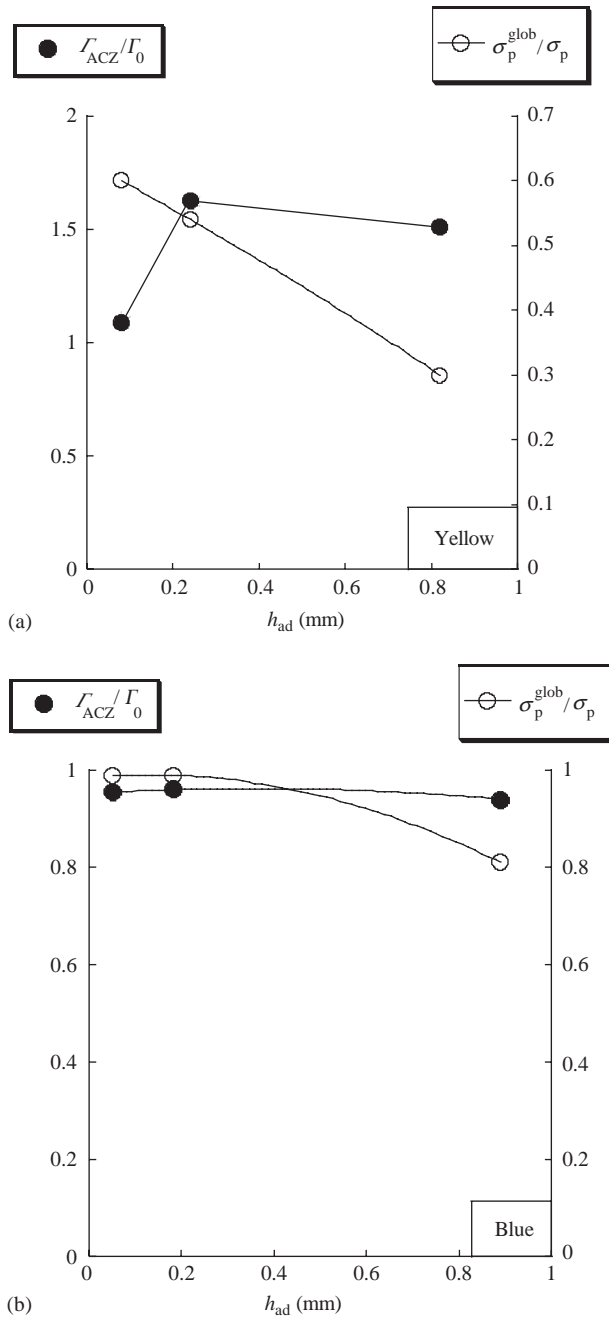


Fig. 10. Variation of the ratio  $\sigma_p^{glob}/\sigma_p$  and  $\Gamma_{ACZ}/\Gamma_0$  for the two adhesives as a function of the bond thicknesses; (a) yellow adhesive; (b) blue adhesive.

cohesive zone parameters, has not been quantitatively addressed in this work but will be qualitatively discussed in Section 5.4.

The length that scales the plastic dissipation is the plastic zone size  $r_y$ , which, for plane strain SSY conditions, is expressed as

$$r_y^{SSY}(\theta) = \alpha(\theta) \frac{1}{3\pi} \frac{E}{1-\nu^2} \frac{\Gamma_0}{\sigma_0^2}, \tag{20}$$

where  $\theta$  is the angle defined with respect to the crack plane (see Fig. 1). For  $\theta = 90^\circ$  (i.e. in order to evaluate the plastic zone height), the plastic zone size is usually significantly larger than for  $\theta = 0^\circ$ . Typically,  $\alpha(90^\circ)$  ranges between 1.25 and 5 depending on the  $T$  stress ( $T$  stress does have a significant effect on plastic zone size, but a relatively small effect on the total dissipation in the plastic zone) and Poisson ratio (see Broberg, 1999, p. 292). For the yellow adhesive, the SSY plastic zone height predicted by Eq. (20) is equal to about 120  $\mu\text{m}$  for  $\alpha = 1$ , while, for the blue adhesive, it is equal to 680  $\mu\text{m}$ . Fig. 11 shows the variation of  $r_y(90^\circ)$  as a function of the adhesive layer thickness computed from the AACZ model. The values at large bond thicknesses agree quite well with the estimate of Eq. (20), considering that  $\alpha$  is equal to about 1.5–2.

### 5.1. Internal constraint

As shown in Figs. 7 and 8, for thin adhesive layers, the global toughness increases linearly with the adhesive layer thickness. The adhesive layer thicknesses of most systems available commercially will fall into that range. As long as the bond thickness is small enough, the adhesive layer will be fully plastic (where the plastic

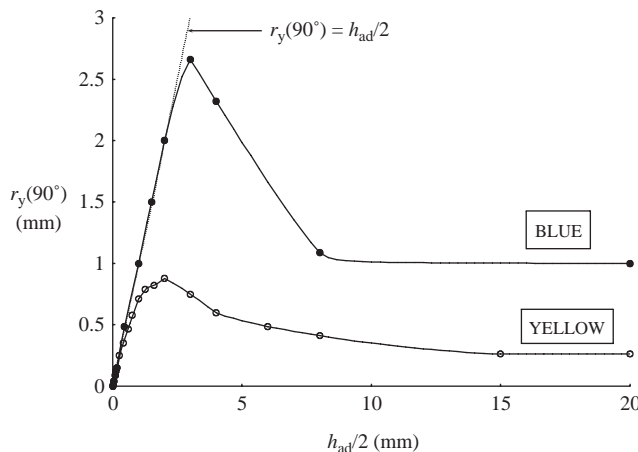


Fig. 11. Variation of the height of the plastic zone as a function of half the adhesive layer thickness for the two adhesives.

zone height is exactly equal to the adhesive layer thickness, see Fig. 9) and the plastic deformation is relatively homogenous through the thickness of the bond. The work of plasticity per unit volume is approximately uniform, and hence the work per unit area  $\Gamma_p$  increases linearly with the adhesive layer thickness. The average effective plastic strain in the fully plastic regime computed with the AACZ model is equal to about 0.012 in the yellow adhesive for the 0.78, 2.34 mm and “K-field” adherents, 0.05 for the thin adherent (0.26 mm), and 0.03 in the blue adhesive. These values are relatively independent of the thickness of the adhesive as long as the bond line thickness is sufficiently small. These values can also be retrieved by noting that  $\Gamma_p$  is approximately equal to

$$\Gamma_p = h_{ad}\sigma_0\langle\bar{\varepsilon}_c^p\rangle\left(\frac{\langle\bar{\varepsilon}_c^p\rangle}{\varepsilon_0}\right)^n. \quad (21)$$

In principle, this approximate analysis offers a means to experimentally evaluate  $\Gamma_0$  by performing tests with different adhesive thicknesses (though thin enough to be fully plastic) in order to separate it from  $\Gamma_p$  using a linear regression<sup>3</sup> :  $\Gamma = \Gamma_0 + \Gamma_p = \Gamma_0 + h_{ad}w_p$ , where  $w_p$  is the mean plastic work per unit volume dissipated in the plastic zone. The fracture work  $\Gamma_0$  is indeed a more intrinsic characteristic of the fracture resistance of the adhesive than  $\Gamma$ .

For larger adhesive thicknesses, the ratio  $\Gamma/\Gamma_0$  increases with the adhesive layer thickness in a non-linear manner. This non-linear evolution corresponds to the fact that the plastic strains become more and more heterogeneous through the adhesive line thickness. As shown in Fig. 9, the joint is no longer fully plastic. The plastic zone is surrounded by an elastic region and the situation becomes an elastic–plastic large-scale yielding problem which is far more complex to analyze than the fully plastic yielding problem (for which simple dimensional or energy arguments can usually be formulated) or the SSY problem (for which one-parameter fracture mechanics solutions exist).

When the adhesive layer becomes sufficiently thick, the ratio  $\Gamma/\Gamma_0$  attains a maximum, which corresponds to the maximum plastic zone height (see Fig. 9), and then decreases to reach the SSY limit where the plastic zone is much smaller than the adhesive thickness. The maximum of  $\Gamma/\Gamma_0$  corresponds to a half-bond thickness of 3 mm in the blue system and 2 mm for the yellow adhesive. These values have no direct correlation with the SSY plastic zone height  $r_y^{SSY}$  (90°).

## 5.2. External constraint

Fig. 8 shows that the bending of thin adherents tends to promote the plasticity in the adhesive layer, which greatly increases the bond toughness. The bending of the thin adherents is associated with large root rotation and large shear

<sup>3</sup>The philosophy of this approach is reminiscent of the essential work of fracture method (see Cotterell and Reddel, 1977; or Pardoën et al., 2004) in which the energy associated to the remote plasticity is separated from the energy spent in the fracture process zone owing to a similarity argument valid when the ligament is fully plastic.

stresses, which tend to promote plastic yielding in the adhesive. Not only are the plastic zones larger, but the magnitudes of the plastic strains are much larger as well. This effect of the adherent thickness (or of the wedge thickness, which also affects the distribution of the shear strain) can be seen in Table 2 for the blue adhesive. Of course, for the blue adhesive, the effect is small simply because the term  $\Gamma_0$  is too large and hides the effect of  $\Gamma_p$  (see Section 5.3). Another reason for the increase of  $\Gamma_p$  in thin adherents arises from the possible extra plastic dissipation associated with the bending of the adhesive layer behind the crack tip. This contribution to the bond toughness is extrinsic and should ideally be extracted from  $\Gamma$  to provide a more physical measure of the global bond toughness (this point is currently under investigation, see Martiny et al., 2005). Note that this contribution is very small except for the thin adherent case ( $h = 0.26$  mm) where it is in the order of the plastic dissipation associated with the crack tip plasticity.

The difference between the “*K*-field” adherent and the wedge peel test with a thick (2.34 mm) adherent is small. In fact, the wedge peel test with thick adherent shows a very large radius of curvature and almost no plasticity in the arms and hence the SSY assumptions are approximately satisfied. The constraint difference due to the change of configuration is very small. Note that the toughness for the *K*-field is found to be much smaller than the maximum toughness for the wedge peel test for the thin adherents.

The calculation with the “*K*-field” adherent was performed with the intention of simulating, within the steady-state framework, the TDCB test on the blue system. The value given in Table 3 for the predicted bond toughness shows that the computed  $\Gamma_p$  value is significant (about 20% of  $\Gamma_0$ ) but remains much smaller than the value expected from the experiments (70% of  $\Gamma_0$ ). We believe that this effect does not come from the use of the *K*-field boundary layer approach but results from the fact that the parameters of the model were identified on tests in which the crack was running near the interface, while in the TDCB the crack was contained in the middle of the layer. It is anticipated that these two situations will involve different plastic zone sizes and different magnitudes of the plastic strains. From a qualitative viewpoint, less plastic dissipation can be expected when fracture occurs near an interface simply because such a crack path leads to half the plastic zone volume associated with a crack running in the middle of the adhesive. The location of the crack path within the adhesive layer can be seen as another source of “internal constraint effect”.

### 5.3. The difference between a high and a low toughness adhesive

The value  $\Gamma_0 = 175 \text{ J/m}^2$  obtained for the yellow adhesive is typical of a high-strength/low-toughness adhesive. The usual rule of thumb for the work of fracture is that

$$\Gamma_0 = \beta \sigma_0 X_0, \quad (22)$$

where  $X_0$  is the relevant microstructural dimension and  $\beta$  is typically 1/2. Introducing the yield stress  $\sigma_{0ad} = 30$  MPa, leads to a value of  $X_0$  in the range of 5–10  $\mu\text{m}$  which agrees quite well with the spacing between the small silica particles (see Fig. A.2c in Appendix A).

The large work of fracture of the blue adhesive,  $\Gamma_0 = 3500$  J/m<sup>2</sup>, results from the cascade of damage events at different scales. If the fracture process was only controlled by the void growth at rubber particles (associated with  $X_0 = 1\text{--}3$   $\mu\text{m}$ ), the predicted fracture work  $\Gamma_0$  would be less than 100 J/m<sup>2</sup>. The large intrinsic toughness  $\Gamma_0$  results from the secondary cracks that dissipate more energy because of the much larger associated length scale (see Fig. A.3 in Appendix A, showing  $X_0 = 200$  to 400  $\mu\text{m}$ ).

Although the plasticity is more extensive in the blue adhesive, the increase of toughness with increasing adhesive layer thickness is less steep than in the yellow adhesive simply because, in the blue adhesive, the intrinsic work of fracture  $\Gamma_0$  is much larger than the plastic contribution  $\Gamma_p$ . In other words, transferability problems associated with different specimen geometries are less crucial when using tough adhesives, especially when keeping the adhesive layer thickness small. Primary structural components that have to be designed against fracture will always be made using tough adhesives. Consequently, integrity assessment procedures based on the minimum bond toughness  $\Gamma = \Gamma_0$ , should not lead to oversized structures because the underestimation of  $\Gamma$  remains small.

#### 5.4. Limitations of the present application of the AACZ model

The application of the AACZ model in this study involves several approximations:

- (i) *The use of rate-independent  $J_2$  flow theory to represent the adhesive behaviour.* Adhesives usually exhibit some degree of strain rate dependence as well as some effect of the hydrostatic stress component on yielding. These effects can be incorporated within the framework of the AACZ model by applying a viscoplastic and/or pressure dependent constitutive model.
- (ii) *It is assumed that  $\Gamma_0$  and  $\sigma_p$  are independent of the local stress state and of the length scale imposed on the separation process by the adhesive thickness.* The effect of the stress state on  $\Gamma_0$  is well known in the “metal ductile fracture” community (Siegmund and Brocks, 1999; Pardoen et al., 2004). When the mechanism of damage involves plastic void growth, slight changes of the stress triaxiality can significantly affect both  $\Gamma_0$  (the term  $\beta$  in Eq. (22) is stress triaxiality dependent) and  $\sigma_p$ . The change of  $\sigma_p$  will in turn also affect the plastic dissipation term  $\Gamma_p$  (Tvergaard and Hutchinson, 1996). In the present problem, larger stress triaxialities are found when the plastic zone encompasses the entire adhesive thickness (leading to a state of uniaxial deformation) than when an elastic zone surrounds the plastic zone. Stress triaxiality is relaxed when the adherents are thin, which induces an increase of the amount of shear near the crack tip. Accounting for constraint effects on the fracture mechanisms requires a more advanced description of the response

of the material within the embedded fracture process zone than the CZ model applied here, such as an extension of the Gurson model adapted to adhesive materials (e.g. the yield surface proposed by Pijenburg and Van der Giessen, 2001, for polymer blends).

Another possible source of constraint appears when the thickness of the adhesive layer interacts with the thickness of the fracture process zone. This geometric constraint directly affects the damage mechanisms. In this case, relationship (22) can no longer be applied since the fracture mechanisms are not able to fully develop to a size of dimension  $X_0$  because the adhesive thickness is of the same magnitude as fracture process length scale  $X_0$ . Interactions between the fracture process zone dimensions and the structural dimensions is frequent in the concrete community but usually not in the metal or polymer communities. As explained in Section 4.3, the poor predictions for the thin adhesive layer thickness in the blue adhesive are certainly related to the interaction between the size of the fracture process zone and the bond line thickness. To date, no well-established constitutive model is available to properly capture such length scale-dependent damage evolutions.

- (iii) *Cracks are assumed to run in the middle of the adhesive.* As discussed in Section 5.2, the location of the crack tip influences the local stress state, the magnitude of the plastic strains as well as the extension of the plastic zone, and hence  $\Gamma_p$ . Also, a moderate mode II component will be associated with a crack running in a “cohesive-near-the-interface” mode. Finally, near interface regions may involve a change of microstructure of the material: adhesive layers may contain gradients of microstructure along the thickness, which might also influence  $\Gamma_0$  (see Lee et al., 2003).

### 5.5. Validity of the ACZ model

Fig. 12 shows the variation of the ratio  $\Gamma_{ACZ}/\Gamma$  as a function of the bond line thickness for different adherent thicknesses. Let us recall that the parameters of the ACZ model were identified so as to provide the same radius of curvature and same crack length as predicted with the AACZ model for a given set of specimen dimensions. Also note that the energy associated with the adhesive layer in the ACZ model,  $\Gamma_{ACZ}$ , was not forced to match the total energy spent within the adhesive layer in the AACZ model,  $\Gamma$ . However, for applicability of the ACZ modelling approach to a wide range of specimen geometries,  $\Gamma_{ACZ}$  should be equal to  $\Gamma$ . For small bond line thickness, the ratio  $\Gamma_{ACZ}/\Gamma$  is in fact close to one, as can be anticipated when comparing the results shown in Figs. 7 or 8 with the results in Fig. 10. However, for large adhesive layer thickness, the ratio  $\Gamma_{ACZ}/\Gamma$  becomes significantly lower than 1 which means that the ACZ model underestimates the bond toughness (assuming that the more detailed AACZ model provides a reliable prediction of what is defined as the “bond toughness”). In other words, it is possible to identify the parameters of a global traction separation curve with the ACZ model that reproduce the experimental crack length and radius of curvature but do not properly capture the total energy spent in fracturing the joint. The situation

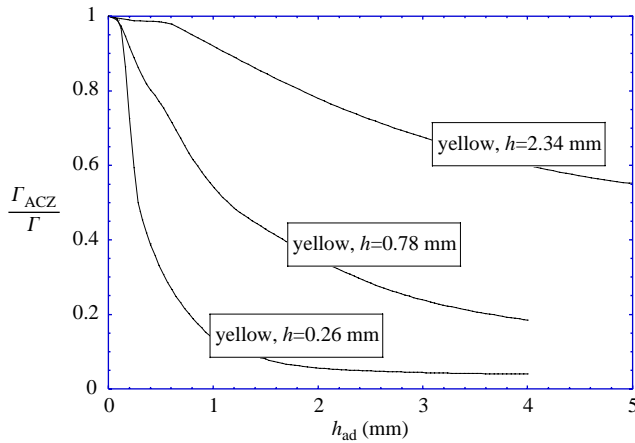


Fig. 12. Variation of the ratio  $\Gamma_{ACZ}/\Gamma$  as a function of the bond line thickness for different adherent thicknesses.

would be different when modelling a regular peel test where the load (and thus the energy) would enter the parameter identification procedure. This point is obviously very important. The implication is that there are circumstances where a two-parameter model, like the ACZ model applied to mode I cracking, is not sufficiently rich to properly represent all the complex and interrelated energy contributions, geometric evolution, and load transfer, even if the adhesive layer thickness is kept constant.

On the other hand, in *thin* adhesive layers made of *tough* or *moderately tough* epoxies, the plastic dissipation in the adhesive layer is small compared to the  $\Gamma_0$  term. In that case, which we believe corresponds to most of the applications addressed until now in the literature (essentially by Thouless and coworkers), the ACZ model can be used safely to assess the integrity of adhesive joints without the need to address the subtleties of constraint effects. The results of Fig. 12 can be interpreted as a demonstration of the limits of the validity of the ACZ approach. Fortunately, these limits of validity agree with the conditions encountered in most practical applications.

### 5.6. Transferability to structures

The transferability to complex bonded structures of data obtained on laboratory specimens will usually prevent the use of the steady-state analysis approach. If the structure is sufficiently complex, the use of the AACZ model becomes unrealistically computationally intensive since it requires very fine meshes to properly capture the plastic dissipation in the adhesive layer. With such an approach, the simulation of long crack advances will be practically impossible. The methodology we envision at this time is to use the AACZ model to address, as in this paper, the complex issues

related to the coupling between the stress state, plastic zone extension, material properties, crack path, and bond line thickness. The AACZ model can also be used in conjunction with well-defined experimental data to calibrate an ACZ model as a function of bond line thickness and as an indicator of the stress state imposed by the adherents.

## Acknowledgements

The authors are very grateful to Prof. A.J. Kinloch (Imperial College, London) for insightful discussions as well as for providing the TDCB samples. Fruitful discussions with Dr. J.-Y. Sener (R&D Cockerill Sambre, Arcelor Group), Dr. F. Lani, M.P. Martiny (Research centre CENAERO, Belgium), Prof. J.G. Williams (Imperial College, London) are also very much appreciated. The technical support of M. Sinnaeve has been essential for the experimental part of this study. Finally, the authors would like to acknowledge the two reviewers for their detailed comments and the interesting points of discussion raised in their reports. This research was made possible owing to the financial support of the Research and Development centre of Cockerill-Sambre, Arcelor Group and of the Walloon region under grant FIRST-doctorat 991/4161. CML is thankful for support from the National Science Foundation through Grant No. CMS-0238522.

## Appendix A.: Microstructural study of debonding mechanisms

*Location of crack front.* As illustrated in Fig. A.1a, in most specimens bonded with the *yellow adhesive*, the crack extends near the middle of the adhesive layer. This path type is commonly designated as “cohesive” debonding. As illustrated in Fig. A.1b, in most *blue adhesive* specimens, the mode of crack extension was “cohesive-near-the-interface”. A small mode II component was thus present along with the opening mode. Fracture surface analysis always revealed the presence of a thin adhesive layer covering the adherent. The crack path was observed in the middle of the adhesive layer only for the thinnest thickness (0.05 mm). Optical examination revealed that the entire layer of blue adhesive was whitened after debonding. In TDCB specimens bonded with the blue adhesive, the fracture was cohesive along the centre of the adhesive layer.

*Micromechanisms.* As shown in Fig. A.2a and b, SEM observation of the fracture surface of the *yellow adhesive* showed the presence of silica particles of different sizes. In most cases, the surface of these particles is flat, typical of cleavage. Fig. A.2b, suggests that the smaller particles do not cleave. No difference was observed for different adherent thicknesses.

Rubber modified epoxies consist of an epoxy matrix with a dispersion of rubber particles. During straining, these particles form microvoids that grow by plastic deformation and coalesce until final fracture. Fig. A.3 shows that the surface morphology of the blue adhesive indeed reveals a multi-scale fracture mechanism. At

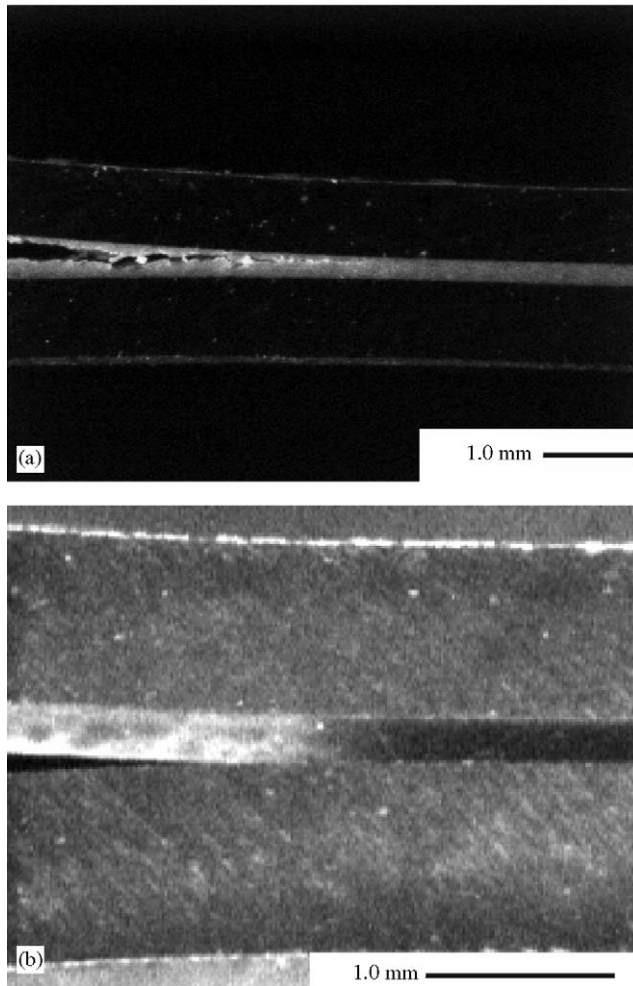


Fig. A.1. Side view of the crack in the (a) yellow adhesive; (b) blue adhesive.

the larger scale, on the “thick” side (Fig. A.3a), the surface exhibits conical marks. The sizes of these marks were typically between 200 and 400  $\mu\text{m}$  in specimens with a standard layer thickness of 0.18 mm. Similar conical marks have been observed on fracture surfaces in PMMA (Andrews, 1968) and in epoxies (e.g. Purslow, 1986). Their formation is explained by the presence of secondary microcracks ahead of the main crack, which grow and eventually link up with the main crack. Due to the presence of heterogeneities and to large damage zones, the secondary cracks do not always nucleate in the plane of the main crack, leading to ribbon-like features, as shown in Fig. A.3b. At higher magnification, small cavities of diameter smaller than 0.5  $\mu\text{m}$  can be observed (see Fig. A.3c). The fracture surface is much flatter on the

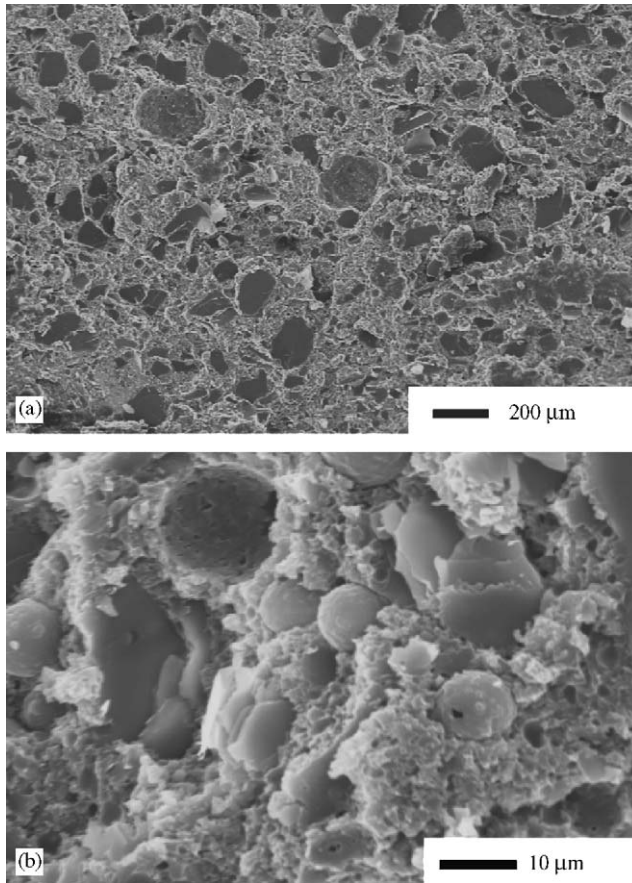


Fig. A.2. (a) Fracture surface of the yellow adhesive; (b) cleaved silica particles.

“thin” (adherent) side than on the thick (adhesive layer) side. In the thinnest blue adhesive layers, the crack propagation was observed to remain along the centre of the adhesive layer and the two fracture surfaces are identical. As can be seen in Fig. A.3d, secondary cracks can then clearly be distinguished on the surfaces but they are no longer “conical”. The density of secondary cracks is larger than in thicker adhesive layers and the size of most secondary cracks is between 100 and 150  $\mu\text{m}$ .

The characteristic features of the TDCB fracture surface are similar to the ones observed for the wedge peel test using the standard adhesive layers thickness of 0.18 mm. However, the length of the secondary cracks is slightly larger  $\approx 400 \mu\text{m}$ . The fracture surface of the bulk blue adhesive (CT specimen) also presents secondary cracks with typical length  $\approx 200 \mu\text{m}$ , although the shape of these secondary cracks is somewhat different.

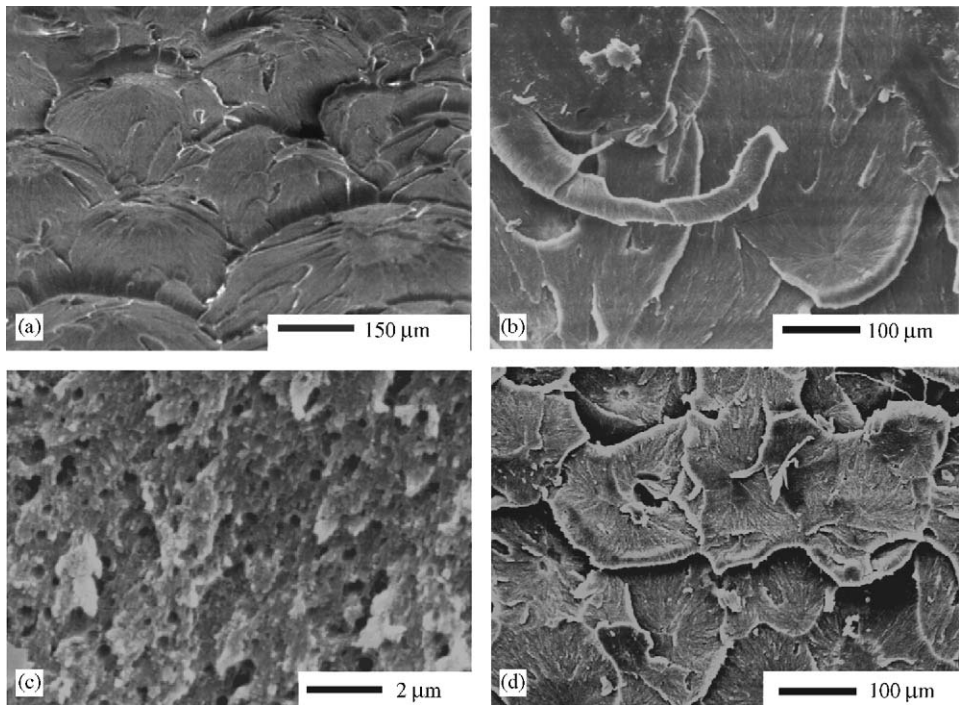


Fig. A.3. (a) Conical secondary crack marks on the fracture surface of the blue adhesive; (b) ribbon in the blue adhesive, suggesting crack bridging; (c) microvoids at high magnification; (d) secondary crack marks on the fracture surface of the thin adhesive layer.

## References

- Andersson, T., Stigh, U., 2004. The stress-elongation relation for an adhesive layer loaded in peel using equilibrium and energetic forces. *Int. J. Solids Struct.* 41, 413–434.
- Andrews, R.D., 1968. *Fracture in Polymers*. Oliver and Boyd, Edinburgh.
- Bascom, W.D., Cottingham, R.L., Jones, R.J., Peyser, P., 1975. The fracture of epoxy and elastomer-modified epoxy polymers in bulk and as adhesive. *J. Appl. Polym. Sci.* 19, 2545–2562.
- Blackman, B.R.K., Kinloch, A.J., 1997. Determination of the mode I adhesive fracture energy,  $G_{Ic}$ , of structural adhesives using the double cantilever beam (DCB) and the tapered double cantilever beam (TDCB) specimens. Version 97-04. ESIS TC4 Protocol.
- Broberg, K.B., 1999. *Cracks and Fracture*. Academic Press, New York.
- Chai, H., 1986. Bond thickness effects in adhesive joints and its significance for mode I interlaminar fracture of composites. In: *Proceedings of the Seventh Conference on Composite Materials Testing and Design*, pp. 209–231.
- Chai, H., 1995. Deformation and fracture of particulate epoxy in adhesive bonds. *Acta Metall. Mater.* 43, 163–172.
- Cotterell, B., Reddel, J.K., 1977. The essential work of plane stress ductile fracture. *Int. J. Fract.* 13, 267–277.
- Daghyani, H.R., Ye, L., Mai, Y., 1995. Mode-I fracture behaviour of adhesive joints. Part II. Stress analysis and constraint parameters. *J. Adhes.* 53, 163–172.

- Dean, R.H., Hutchinson, J.W., 1980. Quasi-static steady crack growth in small-scale yielding. In: *Fracture Mechanics: 12th Conference, ASTM STP 700*, American Society for Testing and Materials, pp. 383–405.
- Ferracin, T., Landis, C.M., Delannay, F., Pardoën, T., 2003. On the determination of the cohesive zone properties of an adhesive layer from the analysis of the wedge peel test. *Int. J. Solids Struct.* 40, 2889–2904.
- Ikeda, T., Yamashita, A., Lee, D., Miyazaki, N., 2000. Failure of a ductile adhesive layer constrained by hard adherends. *J. Eng. Mater. Technol.* 122, 80–85.
- Kafkalidis, M.S., Thouless, M.D., 2002. The effects of geometry and material properties on the fracture of single lap-shear joints. *Int. J. Solids Struct.* 39, 4367–4383.
- Kafkalidis, M.S., Thouless, M.D., Yang, Q.D., Ward, M.S., 2000. Deformation and fracture of an adhesive layer constrained by plastically deforming adherends. *J. Adhes. Sci. Technol.* 14, 1593–1607.
- Kinloch, A.J., 1997. Adhesives in engineering. *Proc. Inst. Mech. Eng.* 211-G, 307–335.
- Kinloch, A.J., 2002. The durability of adhesive joints. In: Dillard, D.A., Pocius, A.V. (Eds.), *The Mechanics of Adhesion*. Elsevier, Amsterdam, pp. 661–695 (Chapter 17).
- Kinloch, A.J., Shaw, S.J., 1981. The fracture resistance of a toughened epoxy adhesive. *J. Adhes.* 12, 59–77.
- Landis, C.M., Pardoën, T., Hutchinson, J.W., 2000. Crack velocity dependent toughness in rate dependent material. *Mech. Mater.* 32, 663–678.
- Lee, D.-B., Ikeda, T., Miyazaki, N., Choi, N.-S., 2003. Fracture behaviour around a crack tip in rubber-modified epoxy adhesive joint with various bond thicknesses. *J. Mater. Sci. Lett.* 22, 229–233.
- Lowe, A., Kwon, O., Mai, Y., 1996. Fatigue and fracture behavior of novel rubber modified epoxy resins. *Polymer* 37, 565–572.
- Madhusudhana, K.S., Narasimhan, R., 2002. Experimental and numerical investigations of mixed mode crack growth resistance of a ductile adhesive joint. *Eng. Fract. Mech.* 69, 865–883.
- Martiny, P., Kinloch, A.J., Lani, F., Landis, C.M., Pardoën, T., 2005. Multiscale modeling of the steady-state fracture of adhesively bonded joints. In: Vorvolakos, K. (Ed.), *Proceedings of the 28th Annual Meeting of The Adhesion Society*, 15–18 February, Mobile, Alabama, USA. The Adhesion Society Inc., pp. 360–362.
- Mohammed, I., Liechti, K.M., 2000. Cohesive zone modeling of crack nucleation in mixed-mode interfacial corners. *J. Mech. Phys. Solids* 48, 735–764.
- Ochi, M., Shimaoka, S., 1999. Phase structure and toughness of silicone-modified epoxy resin with added silicone graft copolymer. *Polymer* 40, 1305–1312.
- Ochi, M., Takemiya, K., Kiyohara, O., Nakanishi, T., 2000. Effect of the addition of aramid–silicone block copolymer on the phase structure and toughness of cured epoxy resins modified with RTV silicone. *Polymer* 41, 195–201.
- Pardoën, T., Hachez, F., Marchioni, B., Blyth, P.H., Atkins, A.G., 2004. Mode I fracture of sheet metal. *J. Mech. Phys. Solids* 52, 423–452.
- Pijnenburg, K.G.W., Van der Giessen, E., 2001. Macroscopic yield in cavitated polymer blends. *Int. J. Solids Struct.* 38, 3575–3598.
- Purslow, D., 1986. Matrix fractography of fibre reinforced epoxy resin. *Composites* 17, 289–301.
- Sener, J.-Y., 1998. Développement de nouvelles méthodologies de mesure de l'adhésion de revêtements sur substrats métalliques, Ph.D. Thesis, UCL.
- Siegmund, T., Brocks, W., 1999. Prediction of the work of separation and implications to modeling. *Int. J. Fract.* 99, 97–116.
- Sorensen, B.F., 2002. Cohesive law and notch sensitivity of adhesive joints. *Acta Mater.* 50, 1053–1061.
- Thouless, M.D., Adams, J.L., Kafkalidis, M.S., Ward, S.M., Dickie, R.A., Westerbeek, G.L., 1998. Determining the toughness of plastically deforming joints. *J. Mater. Sci.* 33, 189–197.
- Tvergaard, V., Hutchinson, J.W., 1992. The relation between crack growth resistance and fracture process parameters in elastic–plastic solids. *J. Mech. Phys. Solids* 40, 1337–1397.
- Tvergaard, V., Hutchinson, J.W., 1994. Toughness of an interface along a thin ductile layer joining elastic solids. *Philos. Mag. A* 70, 641–656.

- Tvergaard, V., Hutchinson, J.W., 1996. On the toughness of ductile adhesive joints. *J. Mech. Phys. Solids* 44, 789–800.
- Wang, R.X., Sinclair, A.N., Spelt, J.K., 2003. Strength of adhesive joints with adherend yielding: II. Peel experiments and failure criteria. *J. Adhes.* 79, 49–66.
- Wei, Y., Hutchinson, J.W., 1998. Interface strength, work of adhesion and plasticity in the peel test. *Int. J. Fract.* 93, 315–333.
- Yang, Q.D., Thouless, M.D., 2001. Mixed-mode fracture analyses of plastically deforming adhesive joints. *Int. J. Fract.* 110, 175–187.
- Yang, Q.D., Thouless, M.D., Ward, S.M., 1999. Numerical simulation of adhesively -bonded beams failing with extensive plastic deformation. *J. Mech. Phys. Solids* 47, 1337–1353.